ARTICLE

Check for updates

Easy-plane spin Hall oscillator

Eric Arturo Montoya [1,2✉], Amanatullah Khan [1], Christopher Safranski [1], Andrew Smith[1] &
Ilya N. Krivorotov [1✉]

Spin Hall oscillators (SHOs) based on bilayers of a ferromagnet (FM) and a non-magnetic heavy metal (HM) are electrically tunable nanoscale microwave signal generators. Achieving high output power in SHOs requires driving large-amplitude magnetization dynamics by a direct spin Hall current. Here we present an SHO engineered to have easy-plane magnetic anisotropy oriented normal to the bilayer plane, enabling large-amplitude easy-plane dynamics driven by spin Hall current. Our experiments and micromagnetic simulations demonstrate that the easy-plane anisotropy can be achieved by tuning the magnetic shape anisotropy and perpendicular magnetic anisotropy in a nanowire SHO, leading to a significant enhancement of the generated microwave power. The easy-plane SHO experimentally demonstrated here is an ideal candidate for realization of a spintronic spiking neuron. Our results provide an approach to design of high-power SHOs for wireless communications, neuromorphic computing, and microwave assisted magnetic recording.

[1] Department of Physics and Astronomy, University of California, Irvine, CA 92697, USA. [2] Department of Physics and Astronomy, University of Utah, Salt Lake City, UT 84112, USA. ✉email: eric.montoya@utah.edu; ilya.krivorotov@uci.edu

Manipulation of magnetization by spin-orbit torques (SOTs) forms the basis of several promising spintronic technologies such as SOT memory (SOT-MRAM)[1–6], SOT oscillators[7–9], neuromorphic computing devices[10–14], and SOT-based magnonic logic[15,16]. Additionally, SOT oscillators serve as a test bed for fundamental studies of strongly nonlinear magnetization dynamics in nanoscale ferromagnets (FMs)[17].

The simplest type of SOT oscillator is the spin Hall oscillator (SHO)[18–23]. SHO is based on a bilayer of an FM and a non-magnetic heavy metal (HM), as illustrated in Fig. 1a. A direct electric charge current in the HM layer flowing along the x-axis gives rise to a pure spin current density j_s along the z-axis (gray
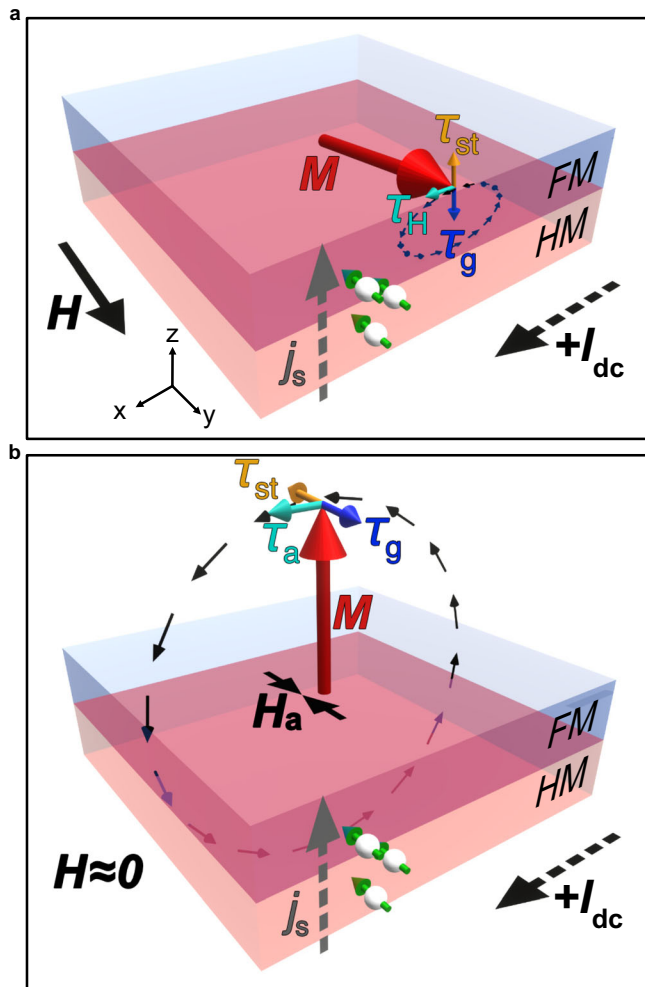

Fig. 1 Spin Hall oscillator dynamics. a Persistent magnetization dynamics in a conventional spin Hall oscillator. Applied direct current I_{dc} leads to spin Hall current j_s (gray dashed arrow) from heavy metal (HM), which applies spin Hall torque τ_{st} (orange arrow) that compensates the Gilbert damping torque τ_g (dark blue arrow) and drives persistent precession (arrows showing elliptical precession trajectory) of the ferromagnet (FM) magnetization **M** (red arrow). The spin current is polarized in the plane of the FM film (green arrows), and an external field **H** is applied to define the precession axis (large black arrow), leading to small-angle precession of magnetization due to the effective field torque τ_H (turquoise arrow). **b** Easy-plane spin torque oscillator dynamics. In this geometry, easy-plane magnetic anisotropy is perpendicular to the FM layer plane, and spin Hall current is polarized perpendicular to the easy plane. Spin Hall torque τ_{st} pulls **M** out of the easy plane, and the anisotropy torque τ_a (turquoise arrow) drives large-amplitude circular magnetization precession around the anisotropy field **H$_a$** that is perpendicular to the easy plane.

dashed arrow) with its magnetic polarization parallel the y-axis (green arrows). Interaction of j_s with the FM magnetization **M** gives rise to spin Hall torque $\tau_{st} \sim j_s$ opposing the Gilbert damping torque τ_g. We use the term polarization to refer to the direction of the electron magnetic moment of spin current.

When j_s exceeds a critical value proportional to the FM Gilbert damping parameter α, τ_{st} overcomes the damping τ_g and excites persistent auto-oscillatory elliptical magnetization precession around the equilibrium direction of **M**. The lowest critical current is observed for **M** magnetized in the $-y$-direction by an applied field **H**.

For easy-plane (EP) magnetic anisotropy coinciding with the FM layer plane, the precession trajectory is elliptical, as shown in Fig. 1a. The precession frequency increases with increasing **H** and the anisotropy field H_a, and decreases with increasing precession amplitude due to the negative nonlinear frequency shift in this geometry[24]. The amplitude of precession first increases with increasing j_s but then saturates at precession cone angles typically not exceeding 20° due to the nonlinear damping mechanism[21,25,26]. The current-driven auto-oscillations of **M** generate microwave voltage due to the FM magnetoresistance. The frequency and amplitude of this microwave voltage depend on j_s, and thus SHOs are electrically tunable microwave signal generators of nanoscale dimensions[24].

SHO generators of microwave signals with high output power and low phase noise are desirable for applications[10,27]. Large-amplitude persistent magnetization dynamics with the precession cone angle of nearly 90° have been predicted for EP FMs upon injection of spin current polarized normal to the easy plane[28–30]. Such type of an EP-SHO with the magnetically easy xz-plane is shown in Fig. 1b. In contrast to the conventional SHO in Fig. 1a, large-amplitude precessional dynamics in EP-SHOs is excited immediately above the critical current[28].

The EP-SHO magnetization is tilted out of the EP by the spin Hall torque τ_{st}, whereupon it processes with large amplitude around the anisotropy field H_a parallel to the y-axis[31]. The critical current for these dynamics is defined by a smaller magnetic anisotropy present within the dominant EP anisotropy rather than by the FM Gilbert damping[28–30]. The EP-SHO can operate in zero external magnetic fields, which is desired for many applications. The EP-SHO system is especially attractive for the realization of a magnetic spiking neuron, as has been proposed in several recent theoretical publications[32–34]. The EP-SHO is predicted to generate a large-amplitude sub-nano-second output voltage pulse in response to an input current pulse exceeding a threshold value. Null output is expected for sub-threshold input pulses. This is the characteristic behavior of a spiking neuron.

Large-amplitude EP persistent dynamics have been theoretically studied in spin-transfer-torque nanopillar devices[30,31] but have yet to be explored in SOT devices, such as SHOs. Here we report the experimental realization of a nanowire EP-SHO based on a Pt|FM bilayer, where FM is a Co|Ni superlattice[35–40]. The EP-SHO dynamics are achieved via tuning the Co|Ni perpendicular magnetic anisotropy (PMA) and the magnetic shape anisotropy of the nanowire to manufacture an easy plane defined by the wire axis and the film normal (xz-plane) as shown in Fig. 2a. We present measurements and micromagnetic simulations demonstrating that the microwave power generated by the SHO is maximized when the magnetic easy-plane energy landscape is realized. Our results are relevant for the engineering of scalable, high-power SHOs for wireless communications[41], neuromorphic computing[12,42,43], room-temperature radio frequency bolometers[27], and microwave-assisted magnetic recording[44].

Results

Device geometry and magnetoresistance. Figure 2a shows a schematic of the nanowire EP-SHO device along with the coordinate
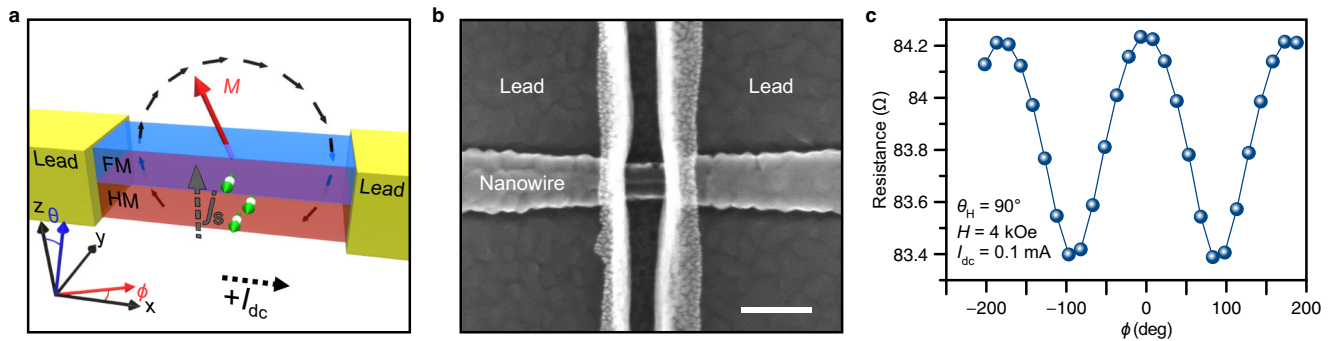
Fig. 2 Device schematics and magnetoresistance. a Schematic of easy-plane spin Hall oscillator (EP-SHO) based on a heavy metal (HM=Pt) and a ferromagnetic metal (FM=Co|Ni superlattice) bilayer nanowire, as well as the Cartesian (x, y, z) and spherical (ϕ, θ) coordinate systems used here. A positive direct charge current in the HM layer $+I_{dc}$ (black dashed arrow) generates a spin Hall current $\mathbf{j}_s$ (gray dashed arrow) flowing in the z-direction with its polarization in the $-y$-direction (green arrows). Spin current $\mathbf{j}_s$ impinging on the FM applies spin Hall torque τ_{st} to magnetization $\mathbf{M}$ and pulls it out of the easy xz-plane. The magnetization then precesses about the easy-plane anisotropy field $\mathbf{H}_a \| y$ as indicated by black arrows. **b** Scanning electron micrograph of an EP-SHO. The scale bar is 100 nm. **c** Resistance of the EP-SHO device in **b** as a function of a 4 kOe (400 mT) magnetic field direction in the xy-plane measured at $T = 4.2$ K.

system used in this article. An applied direct electric current flowing in HM Pt along the length of the nanowire (x-direction) leads to a transverse spin Hall current[45] flowing in the z-direction that is polarized in the $-y$-direction. When injected into the FM, the spin Hall current applies spin Hall torque to the FM magnetization[46] and drives auto-oscillatory magnetization dynamics[7].

The EP-SHO nanowires studied here were patterned from substrate||seed|HM|FM|cap films deposited by magnetron sputtering (see Methods and Supplementary Note 1). We used Pt (7 nm) for the HM layer and a $[Co(0.98 \text{ nm})|Ni(1.46 \text{ nm})]_2|Co(0.98 \text{ nm})$ superlattice as the FM layer. The Co|Ni superlattice was selected for its large anisotropic magnetoresistance (AMR) and tunability of PMA via the Co and Ni layer thicknesses[47]. Highly resistive Ta is employed for the seed (3 nm) and capping (4 nm) layers[48]. Electron beam lithography and Ar$^+$ ion milling were used to define 50 nm wide, 40 μm long nanowires from the film stack. Ta(5 nm)|Au(40 nm)|Ta(5 nm) electric leads were attached to the nanowire with the inter-lead gap varying from 50 to 450 nm. The spacing between the leads defines the active region of the nanowire where current density exceeding the critical value for the excitation of auto-oscillations can be achieved. Figure 2b shows a scanning electron micrograph of a typical EP-SHO device.

In this article, we study and compare two types of SHOs: the standard SHO (S-SHO), similar to that shown in Fig. 1a, and the EP-SHO. In the S-SHO configuration, moderate-amplitude auto-oscillatory dynamics are driven by the antidamping spin Hall torque around the effective magnetic field often dominated by the applied field $\mathbf{H}$.

The maximum antidamping spin Hall torque efficiency in this configuration is achieved for a saturating field $\mathbf{H}$ applied parallel to the direction of the spin Hall current polarization (along the y-axis: $\theta = 90°$, $\phi_H = 90°$)[49]. However, the maximum efficiency of converting magnetization oscillations to resistance oscillations due to AMR oscillations is achieved at $\phi = 45°$. For this reason, the external field is usually applied at an angle between $\phi_H = 45°$ and $\phi_H = 90°$ as a compromise[50].

In the EP-SHO configuration, the applied field H is nearly zero, and the energy landscape is dominated by internal fields: shape anisotropy and PMA. The goal is to artificially manufacture an EP in the xz-plane, such that spin Hall current from the Pt underlayer is polarized orthogonal to the EP. In this case, the spin Hall torque pushes the magnetization out of the EP, where it precesses about the effective EP field, as shown in Fig. 2a.

Magnetic shape anisotropy for a nanowire of rectangular cross section can be approximately described via demagnetization fields

along the three principal axes: $H_{D_x} = -4\pi D_x M_x$, $H_{D_y} = -4\pi D_y M_y$, and $H_{D_z} = -4\pi D_z M_z$, where D_i are the demagnetization factors and M_i are the magnetization components in the $i = x, y, z$-directions. The saturation magnetization of the Co|Ni superlattice is estimated from thickness dependent FMR measurements to be $M_s \approx 997$ emu cm^{-3} (997 kA m^{-1}) (Supplementary Note 2). The demagnetization factors for the Co|Ni nanowire used here can are calculated using analytical expressions[51]: $D_x = 1.4 \times 10^{-4}$, $D_y = 0.121$, and $D_z = 0.879$. Upon patterning the nanowire, the y-axis becomes a hard magnetic axis with a maximum demagnetization field of $H_{D_y} = 1.52$ kOe ($\mu_0 H_{D_y} = 152$ mT), while the x-axis has a maximum demagnetization field of only a few Oe. The demagnetization field in the direction perpendicular-to-the-film plane is $H_{D_z} = 11.0$ kOe ($\mu_0 H_{D_z} = 1.10$ T). The PMA field H_{PMA} is always in the opposite direction as H_{D_z}; therefore to achieve an easy xz-plane, we require the $H_{PMA} = H_{D_z} = 11.0$ kOe ($\mu_0 H_{PMA} = 1.10$ T) in order to compensate the demagnetization field along the z-axis.

To characterize the H_{PMA} in the magnetic multilayers used here, we made broadband ferromagnetic resonance measurements (FMR)[52] prior to patterning of the multilayers into the nanowire devices. Using these measurements, we adjusted the Co and Ni layer thicknesses such that the sum of Pt|Co and Co|Ni interfacial PMA contributions at room temperature is less than, but nearly compensates the demagnetization field in the z-direction, as described in Supplementary Note 2. Furthermore, we find the PMA of the multilayer increases by 12% upon cooling from 295 K to 4.2 K as discussed in the Supplementary Note 3. For this reason, the equilibrium direction of magnetization in our nanowire devices at 4.2 K is along the z-axis. However, this uniaxial anisotropy is small and the dominant anisotropy is the easy-xz-plane anisotropy. Furthermore, this small z-axis uniaxial anisotropy can then be continuously tuned by temperature from easy-z-axis to easy-x-axis, achieving perfect easy-xz-plane anisotropy at the transition temperature. In this work, we tune the temperature via Joule heating by the applied direct current.

In this article, we report measurements of a SHO device with an active region length $l = 145$ nm made at $T = 4.2$ K. This device was chosen because its impedance is similar to that of our 50 Ω microwave circuitry. Figure 2c shows the resistance of the EP-SHO device as a function of in-plane angle ϕ_H ($\theta_H = 90°$) of applied magnetic field $H = 4$ kOe ($\mu_0 H = 400$ mT) and a small probe current of $I_{dc} = 0.1$ mA. From measurements of a similar
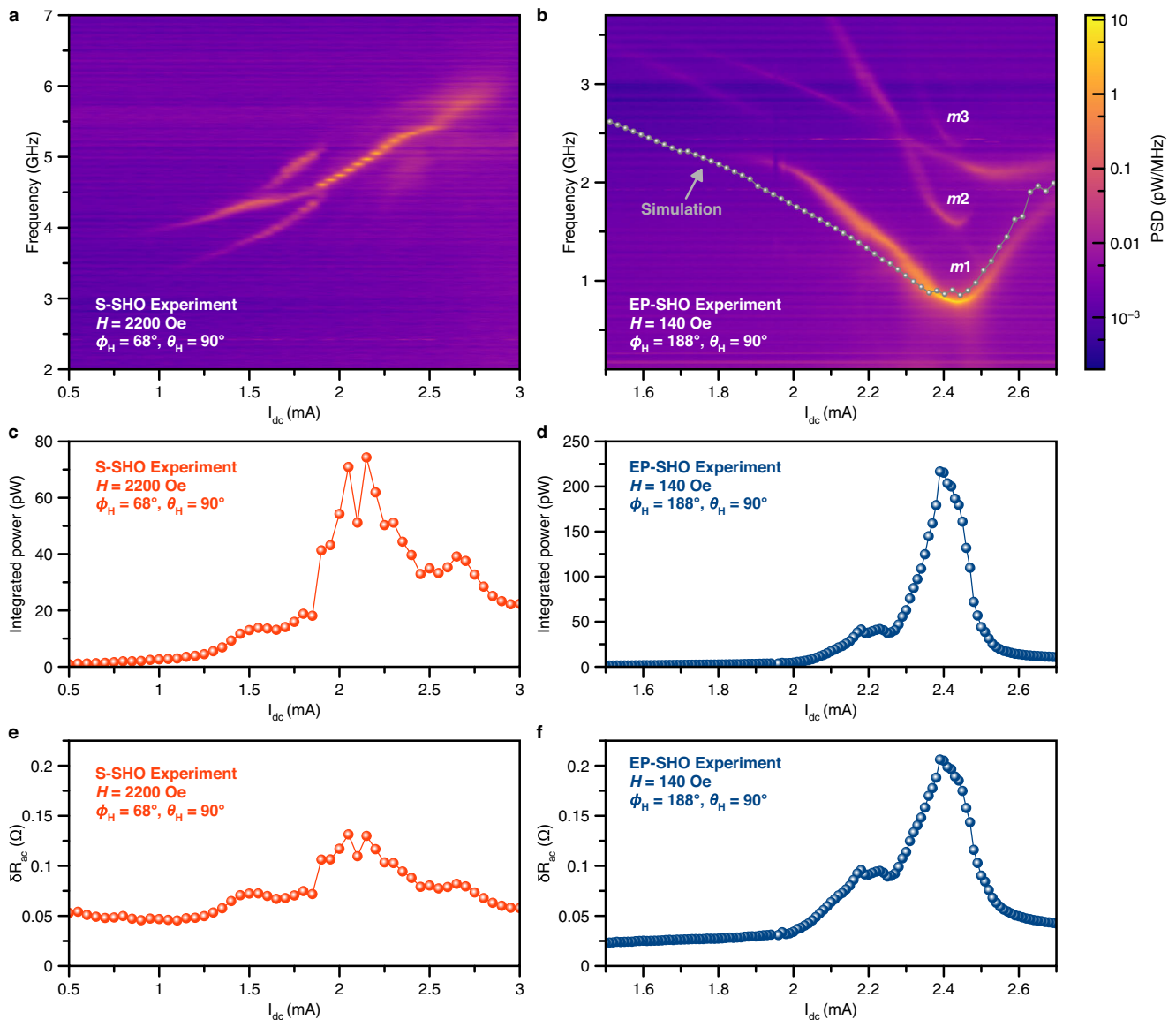
Fig. 3 Microwave signal emission. Power spectral density (PSD) of microwave signal generated as a function of applied direct current I_{dc} for the **a** high-field standard spin Hall oscillator (S-SHO) configuration and **b** low-field easy-plane spin Hall oscillator (EP-SHO) configuration. The lowest energy mode and its second and third harmonics are labeled $m1$, $m2$, and $m3$, respectively. Results from corresponding micromagnetic simulations (see Fig. 3b) are shown as gray curve. Integrated power for the **c** S-SHO and **d** EP-SHO. The amplitude of resistance oscillations for the **e** S-SHO and **f** EP-SHO. ϕ_H and θ_H indicate the angle of applied field H following the coordinate system shown in Fig. 2a.

device, we find the magnetoresistance to be due to both AMR and spin Hall magnetoresistance (SMR)[53,54] with approximately equal contributions.

Microwave emission experiment. The auto-oscillatory magnetization dynamics in SHO devices are excited by spin Hall torque[55] from a direct current I_{dc} exceeding a critical value I_c. These magnetization auto-oscillations give rise to the device resistance oscillations due to AMR and SMR with the amplitude δR_{ac} and to a microwave voltage with the amplitude $V_{ac} \sim I_{dc}\delta R_{ac}$[56].

We first study the S-SHO configuration shown in Fig. 1a achieved by the application of a large magnetic field $H = 2.2$ kOe ($\mu_0 H = 220$ mT) in the plane of the sample at $\phi_H = 68°$, $\theta_H = 90°$. Figure 3a shows power spectral density (PSD) measured in this S-SHO configuration as a function of I_{dc}. The dynamics show a blue frequency shift with increasing I_{dc} above the critical current $I_c = 1$ mA. The observed blue frequency shift is a nonlinear effect

expected for the case of a saturating magnetic field applied perpendicular to the easy plane[24,57]. Figure 3c shows the total integrated microwave power P generated by the SHO as a function of I_{dc}. The integrated power versus I_{dc} is non-monotonic and peaks at $P = 74$ pW near $I_{dc} \approx 2.15$ mA. All values of microwave power given in this article are those delivered to a standard 50 Ω load.

We next measure the same device in a nearly zero external magnetic field—a configuration allowing us to achieve the EP-SHO regime of operation. In the EP-SHO configuration, the energy landscape is dominated by PMA and the shape anisotropy fields. Figure 3b shows measured PSD as a function of I_{dc} for $H = 140$ Oe ($\mu_0 H = 14$ mT) and ($\phi_H = 188°$); similar results were found for other small applied field values. A low-frequency auto-oscillatory mode labeled $m1$ is excited for currents exceeding $I_{dc} = 1.8$ mA. In contrast to the standard high-field SHO regime, the emission frequency initially red-shifts with increasing I_{dc} and reaches a minimum of 0.78 GHz at $I_{dc} \approx 2.44$ mA. For $I_{dc} > 2.44$

mA, the emission frequency blue-shifts. Figure 3d shows the integrated power of the SHO in this low-field regime as a function of I_{dc}. A non-monotonic dependence of microwave emission power is observed with the maximum value of 217 pW reached at $I_{dc} = 2.39$ mA, near the frequency minimum. We also observe the 2nd and 3rd harmonics of the mode $m1$, labeled as $m2$ and $m3$ in Fig. 3b. The presence of the harmonics is indicative of large-amplitude nonlinear oscillations of magnetization. A higher-order mode not harmonically related to $m1$ is observed at frequencies near $m2$ and $m3$.

The non-monotonic SHO frequency dependence on I_{dc} in the low-field regime of Fig. 3b is due to the tuning of H_{PMA} by Joule heating, which alters the energy landscape in the xz-plane as shown in Fig. 4. With increasing temperature, the PMA is reduced. For $I_{dc} < 2.4$ mA, the perpendicular anisotropy field dominates the z-axis demagnetization field $H_{PMA} > H_{D_z}$ and the energy landscape can be described as a dominant easy xz-plane anisotropy with a secondary easy z-axis anisotropy within the xz-plane, as shown in Fig. 4a. For $I_{dc} > 2.5$ mA, the reduced H_{PMA} can no longer compensate H_{D_z}, and the energy landscape becomes easy-xz-plane with a secondary easy x-axis, as shown in Fig. 4c. The perfect easy xz-plane characterized by $H_{PMA} = H_{D_z}$ is achieved at the value of $I_{dc} = 2.5$ mA, as shown in Fig. 4b. Figure 3 shows that the microwave power $P = 217$ pW in this EP-SHO regime is significantly enhanced compared to the maximum power $P = 74$ pW in the S-SHO configuration. These output power levels exceed those previously demonstrated in nanowire S-SHOs without significant PMA (25 pW[21]) and in nano-constriction SHOs (28 pW[58]).

The amplitude of resistance oscillations $\delta R_{ac}(\delta R_{ac}^{rms} = \delta R_{ac}/\sqrt{2})$ shown in Fig. 3e and f for the S-SHO and EP-SHO, respectively, are calculated as[19]:

$$\delta R_{ac} = \frac{R(I_{dc}) + R_{50}}{|I_{dc}|} \left(\frac{2P}{R_{50}}\right)^{\frac{1}{2}}, \tag{1}$$

where $R_{50} = 50\,\Omega$ is the load impedance and $R(I_{dc})$ is the resistance of the nanowire at current I_{dc} (Methods).

Micromagnetic simulations. Micromagnetic simulations of current-driven magnetization dynamics for both the S-SHO and the EP-SHO configurations are carried out using Mumax3 micromagnetic code[59] at $T = 0$ K. Geometry, cell-size, and material parameters used in these simulations are listed in "Methods" and experimental measurement of material parameters are discussed in Supplementary Note 2. Technical details of the simulations are given in Supplementary Note 3.

Spin Hall torque is applied to the 145 nm long active region in the middle of the nanowire. In addition, we account for the

current-induced Oersted field and Joule heating. The Oersted field applied to the FM magnetization in the $-y$ direction arises from the electric current in the Pt layer. In Supplementary Note 3, we show that the magnitude of this field is 66.9 Oe per mA I_{dc} (6.69 mT per mA I_{dc}). We also take into account the current-induced reduction of H_{PMA} via Joule heating in the SHO active region. Outside the active region, we assume PMA to be equal to its film value at $T = 4.2$ K, $H_{PMA} = 11.7$ kOe ($\mu_0 H_{PMA} = 1.17$ T). This value of PMA results in the z-axis being the easy axis within the easy-xz-plane outside of the active region. In the active region, H_{PMA} ($\mu_0 H_{PMA}$) is assumed to be a linearly decreasing function of I_{dc} with the experimentally determined slope of -494 Oe mA^{-1} (-4.94 T A^{-1}) as described in Supplementary Note 3. The combination of the Oersted field and reduced H_{PMA} in the active region creates a magnetic potential well for spin waves, resulting in the localization of the auto-oscillatory dynamics to the active region, as observed in our simulations.

We first simulate the S-SHO configuration by applying in-plane external field $H = 2.2$ kOe ($\mu_0 H = 220$ mT) at $\phi_H = 68°$ and $\theta_H = 89.9°$. The tilt of the external field by $0.1°$ away from the film plane is used to eliminate simulation artifacts possible in highly symmetric systems. The system is initialized to uniform magnetization along ϕ_H and then relaxed to its minimum energy state prior to turning on the spin Hall torque. We conduct a series of simulations for applied currents in the range from $I_{dc} = 0.5$ mA to 3.0 mA. The resulting x and y components of the dynamic magnetization, $m_x(t)$ and $m_y(t)$, are used to calculate variation of the sample resistance with time due to AMR and SMR,

$$R_{ac}(t) = \Delta R_{AMR}\langle m_x(t)\rangle^2 - \Delta R_{SMR}\langle m_y(t)\rangle^2, \tag{2}$$

where $\Delta R_{AMR} = 0.4\,\Omega$ is the experimentally measured magnitude of AMR, $\Delta R_{SMR} = 0.4\,\Omega$ is the experimentally measured magnitude of SMR, and $\langle\dots\rangle$ represents averaging over the active region of SHO.

Figure 5a shows the spectra of the current-driven auto-oscillatory dynamics calculated via fast Fourier transforms (FFT) of $R_{ac}(t)$. This figure shows that auto-oscillatory dynamics appear at I_{dc} exceeding 1.25 mA. The magnitude of the resistance oscillations strongly increases when I_{dc} exceeds 2.25 mA. For $I_{dc} > 2.25$ mA, the observed auto-oscillatory mode exhibits a nonlinear blue frequency shift. Figure 5c shows the amplitude of resistance oscillations δR_{ac} versus I_{dc}.

Simulations in the EP-SHO dynamics were made for $H = 140$ Oe ($\mu_0 H = 14$ mT), $\phi_H = 188°$, and $\theta_H = 89.9°$. These simulations revealed the bi-stable behavior of the system in the presence of I_{dc}: at a fixed current above the critical, the system can be either in a dynamic state of large-amplitude magnetization oscillations or in a static state. An example of this behavior is
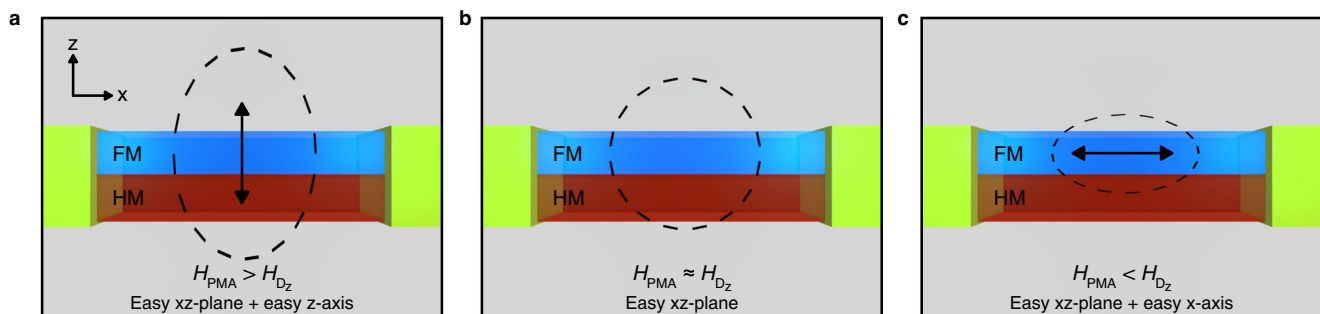

Fig. 4 Easy plane energy landscape. Figures show the xz-plane side view of bilayer ferromagnet (FM) and non-magnetic heavy metal (HM) nanowire devices. Dashed ellipsoids show constant energy contours of magnetization in the easy xz-plane, and double-headed arrows indicate the easy axis. **a** When the perpendicular anisotropy field H_{PMA} is larger than the demagnetization field H_{D_z}, z-axis is an easy axis within the dominant xz easy plane. **b** When $H_{PMA} = H_{D_z}$, perfect easy plane anisotropy is realized in the xz plane. **c** For $H_{PMA} < H_{D_z}$, x-axis is an easy axis within the dominant xz easy plane.
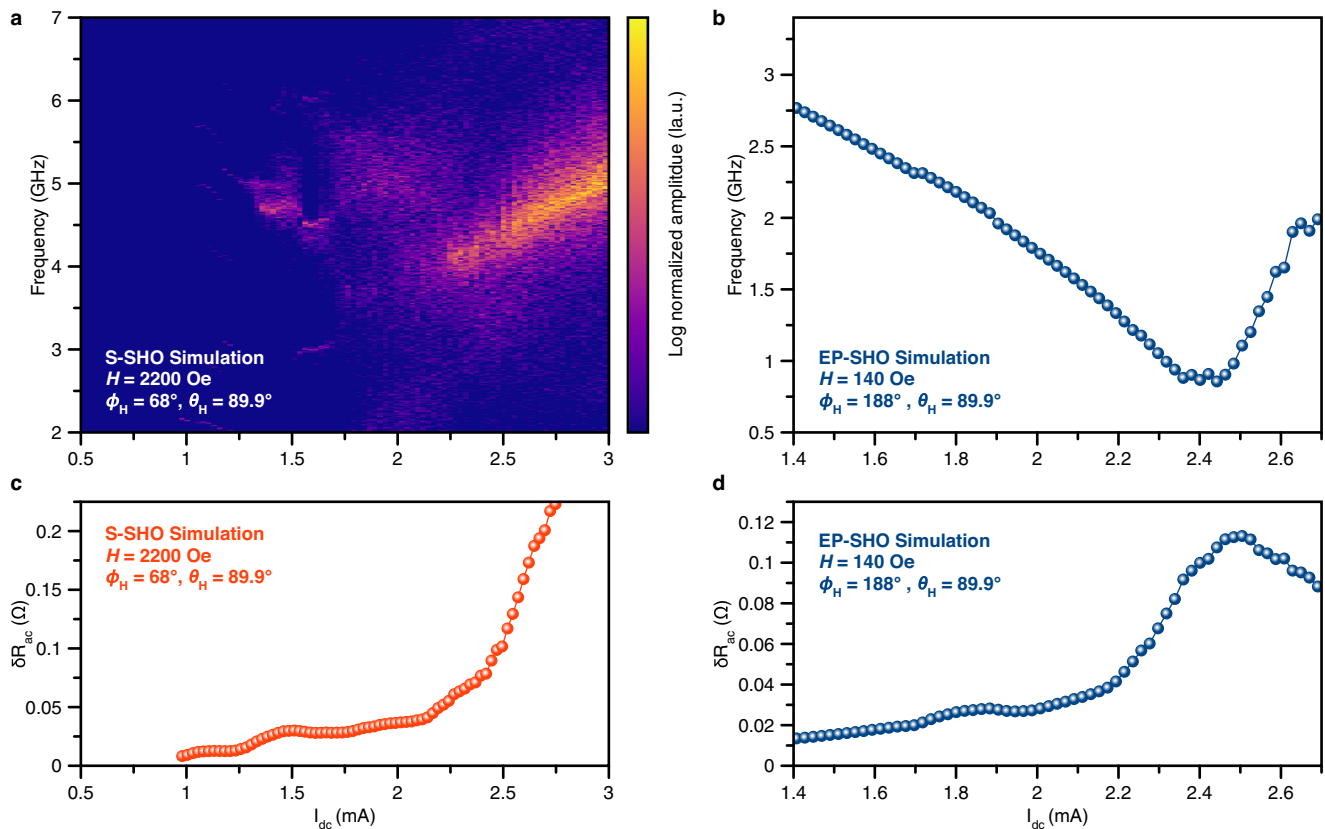
Fig. 5 Micromagnetic simulation of spin-orbit torque nano-oscillator. Figures show analysis of micromagnetic simulation data of resistance auto oscillations at each value of applied direct current I_{dc} **a** for high field standard spin Hall oscillator (S-SHO) configuration (via FFT) **b** for low field easy-plane spin Hall oscillator (EP-SHO) configuration (via time domain analysis). Calculated amplitudes of resistance oscillations for **c** high-field S-SHO and **d** low-field EP-SHO. ϕ_H and θ_H indicate the angle of applied field H following the coordinate system shown in Fig. 2a.

shown in Supplementary Fig. S5. We thus expect that the system may exhibit random telegraph switching between the dynamic and the static states. While such switching is detrimental to the operation of this device as a coherent microwave source and must be suppressed via design improvements, it may be beneficial for the operation of the device as a neuron because small external stimuli result in large-amplitude output voltage spikes[10,32,34]. This type of random telegraph noise between large-amplitude dynamics and static states has been previously observed in spin transfer torque oscillators based on nanopillar spin valves[60].

The bi-stability of the dynamic and static states in the EP-SHO regime warrants the use of the time domain analysis described in Supplementary Note 3 instead of the FFT analysis in order to determine the amplitude of magnetization and resistance oscillations in the dynamic state. Figure 5b shows the bias current dependence of the auto-oscillation frequency determined from this analysis. The data reveals a frequency minimum arising from the heating-induced rotation of the easy axis between the z and x axes. These simulation data are in excellent agreement with the experiment, as illustrated by the nearly perfect overlap of the micromagnetic and experimental data in Fig. 3b.

Figure 5d shows the amplitude of resistance oscillations δR_{ac} versus I_{dc} given by our micromagnetic simulations in this EP-SHO regime (see Supplementary Note 3 for details). The data show that the amplitude of resistance oscillations is maximized near the frequency minimum where the perfect easy-xz-plane anisotropy is realized. This non-monotonic dependence of the amplitude of auto-oscillations on I_{dc} is expected for the EP-SHO dynamics and is consistent with the experimental data in Fig. 3f.

Supplementary Movie 1 shows the spatially resolved time evolution of current-driven magnetization dynamics given by our micromagnetic simulations for $I_{dc} = 2.44$ mA, which corresponds to the maximum of $\delta R_{ac}(I_{dc})$. Figure 6a–c shows three snapshots from this Movie within one period of the auto-oscillations. Figure 6a shows the dynamic micromagnetic state in the active region at $t = 20.18$ ns after the application of spin Hall torque. At this time, the magnetization in the active region points predominantly in the $+z$-direction. The magnetization in the active region subsequently processes towards the $+x$-direction, as shown in Fig. 6b at $t = 20.69$ ns. These dynamics are consistent with those expected for an ideal EP-SHO shown in Fig. 1b. The next expected stage of the ideal EP-SHO dynamics is the precession of magnetization towards the $-z$-direction. Instead of these ideal dynamics, the magnetization of the nanowire EP-SHO rotates towards the $-y$-direction, as shown in Fig. 6c at $t = 20.93$ ns. From here, the magnetization precesses toward the $-x$-direction before returning to the $+z$-direction, just like in the case of the ideal EP-SHO in Fig. 1b. This precession cycle repeats with small cycle-to-cycle variations of the micromagnetic states, as may be expected for a nonlinear dynamical system with many degrees of freedom[61].

Supplementary Movie 2 shows the auto-oscillatory dynamics of the magnetization vector averaged over the EP-SHO active region. Figure 6d displays a frame from this Movie showing the path traced by the averaged magnetization vector for two consecutive cycles of precession. Figure 6d illustrates that large-angle dynamics expected for an EP-SHO are indeed excited by spin Hall torque. However, compared to the ideal EP-SHO, these dynamics are limited to the $+z$ half-space. This departure from the ideal EP-SHO dynamics is due to exchange coupling to the
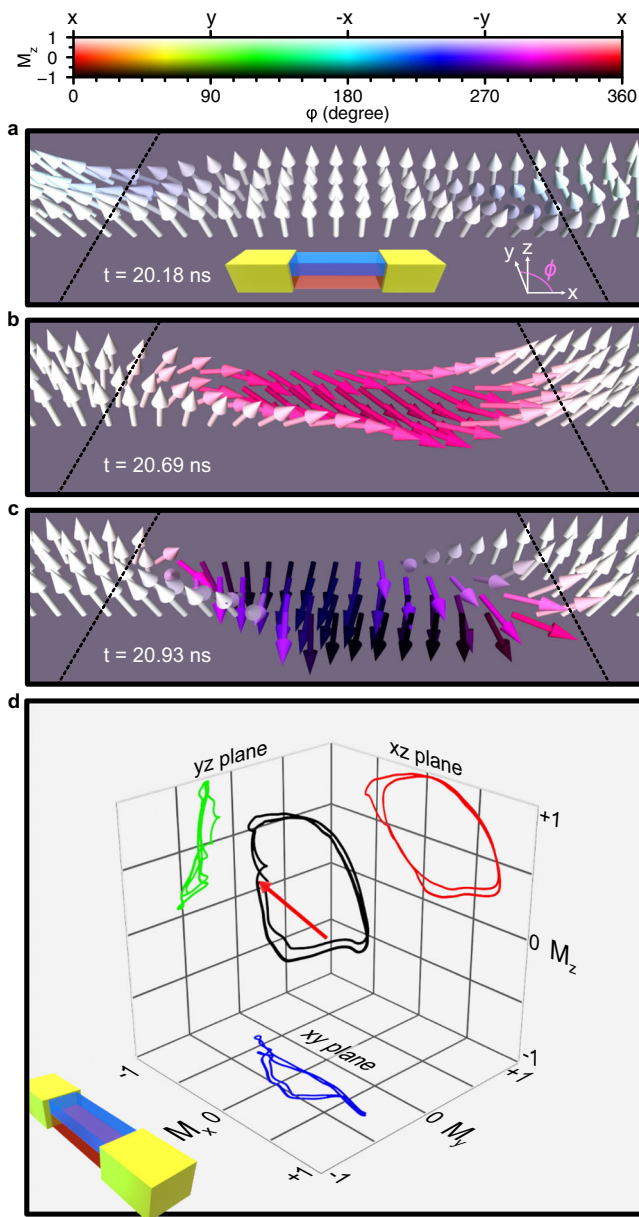
Fig. 6 Micromagnetic snapshots of easy-plane spin Hall oscillator (EP-SHO) auto-oscillations at applied direct current $I_{dc} = 2.44$ mA.
a Magnetization starts from predominantly $+z$-direction at $t = 20.18$ ns, **b** then processes toward the $+x$-direction at $t = 20.69$ ns, **c** subsequently rotates toward the $-y$-direction at $t = 20.93$ ns. Black dashed lines indicate the boundaries of the active region. **d** Average magnetization of the active region traced over two periods of auto-oscillations. ϕ indicates the in-plane angle of the local magnetic moment, following the coordinate system shown in Fig. 2a.

static magnetization outside of the active region that is magnetized along the $+z$-direction. Supplementary Movie 3 and Supplementary Fig. 6 show the corresponding S-SHO auto-oscillatory dynamics of the magnetization vector averaged over the S-SHO active region.

Discussion
Our experimental data in Fig. 3 demonstrate that the easy-plane regime of SHO operation results in a significant power boost compared to the conventional SHO regime. For the nanowire

SHO geometry, we observe a power increase by a factor of three in the EP-SHO regime. Micromagnetic simulations of magnetization dynamics for the EP-SHO and the S-SHO regimes are in qualitative agreement with the experimental observations.

We find full quantitative agreement between the measured and simulated dependence of the EP-SHO generation frequency as a function of direct current bias I_{dc}, as shown in Fig. 3b. The frequency minimum in these data is observed at the bias current corresponding to the perfect easy-xz-plane anisotropy achieved via PMA tuning by Ohmic heating.

The experimentally measured dependence of the amplitude of resistance oscillations δR_{ac} on I_{dc} in the EP-SHO regime shown in Fig. 3f is qualitatively similar to that given by the simulations in Fig. 5d: in both cases, the auto-oscillation amplitude maximum is observed near I_{dc} corresponding to the perfect easy-xz-plane anisotropy. However, the experimentally measured auto-oscillation amplitude is higher than that predicted by the simulations. We attribute this discrepancy to weak exchange coupling between crystallographic grains of the FM film. The reason for the auto-oscillation amplitude being limited to the $+z$ half-space in the simulations is strong exchange coupling to static magnetization outside of the active region. Therefore, a decrease of exchange coupling to the static magnetization is expected to extend the auto-oscillatory dynamics into the $-z$ half-space, increase δR_{ac}, and bring the auto-oscillations closer to the ideal EP-SHO shown in Fig. 1b. Recent studies clearly demonstrate significant granularity in Co|Ni superlattices deposited by magnetron sputtering and the associated weakening of the inter-grain exchange in such films[62].

The observed excursion of the auto-oscillating magnetization into the $-y$-direction seen in Fig. 6d enhances the amplitude of resistance oscillations due to the SMR term in Eq. (2). Such SMR contribution to the resistance oscillations is absent in an ideal EP-SHO in Fig. 1b where large-amplitude circular dynamics in the xz-plane is expected. Therefore we do not expect significant microwave power generated by an ideal EP-SHO at the frequency of its magnetization auto-oscillations. However, the ideal EP-SHO would produce large-amplitude microwave power at twice the magnetization auto-oscillation frequency due to the AMR term in Eq. (2). Such large-amplitude second-harmonic microwave emission may be beneficial for applications requiring high-frequency microwave signals. The output power of the EP-SHO can be further boosted in a 3-terminal device geometry by embedding a magnetic tunnel junction with large tunneling magnetoresistance on top of the EP-SHO active region in a manner similar to that demonstrated for S-SHOs [7,63].

A recent paper[34] presented micromagnetic simulations of auto-oscillatory dynamics in a geometry similar to that studied here. The auto-oscillatory dynamics found in these simulations are similar to those in an ideal EP-SHO shown in Fig. 1b. These simulations assume the same value of PMA in the active region and outside of the active region, which is challenging to realize due to the enhanced Ohmic heating of the active region. Our simulations show that the inclusion of the enhanced heating-induced PMA reduction in the active region may decrease the amplitude of the auto-oscillations of EP-SHO compared to the ideal case.

We also find qualitative agreement between the experiment and simulations for the high-field S-SHO regime. The frequency in the S-SHO regime is found to blue shift with increasing I_{dc} in the experiment (Fig. 3a), and a clear blue frequency shift is seen in the simulations for $I_{dc} > 2.25$ mA as shown in Fig. 5a. This blue shift is a nonlinear dynamical effect expected for a spin torque oscillator with an easy plane magnetic anisotropy and saturating applied magnetic field with a large component perpendicular to the easy plane[24,57].

However, the auto-oscillation frequency seen in the experiment is approximately 1 GHz higher than that predicted by the simulations. This discrepancy is explained by the assumption of the ideal magnetic edge of the nanowire used in the simulations: the simulations assume that the FM material properties at the nanowire edge are the same as in the middle of the wire. This assumption has been previously shown to be incorrect in real devices[19,64] due to the non-ideal properties of the magnetic edge, such as edge roughness[65] and magnetic edge dilution[66]. It has been previously shown that the experimentally measured frequency of spin-wave modes in transversely magnetized thin-film nanowires is higher than expected due to the magnetic edge modification[67]. The magnetic edge modification is also likely to be responsible for deviations of the measured S-SHO frequency from the simulations in the low-bias current regime $I_{dc} < 2.25$ mA. The magnetic edge modification has the largest impact on the spin wave frequency for magnetization saturated near the y-axis[67]. This is the reason for the much smaller impact of this effect on auto-oscillation frequency in the EP-SHO regime.

In the high-field regime of S-SHO operation, the simulations predict a continuous increase of the auto-oscillation amplitude δR_{ac} with increasing I_{dc} up to the largest currents used in the simulations, as shown in Fig. 5c. In contrast, the experimentally measured $\delta R_{ac}(I_{dc})$ shown in Fig. 3e has a maximum near $I_{dc} = 2.15$ mA. The experimentally observed non-monotonic dependence $\delta R_{ac}(I_{dc})$ is consistent with previous studies of S-SHOs[7,50]. The decrease in the auto-oscillation amplitude in the high current regime has been previously observed in S-SHO nanowire devices and explained[21] via nonlinear magnon scattering[68] of the auto-oscillatory mode to thermal magnons. The population of thermal magnons increases in the high-current regime due to the unavoidable Joule heating, resulting in an enhancement of the nonlinear scattering from the auto-oscillatory mode and the associated decrease of its amplitude.

Micromagnetic simulations do not account for thermal magnons, and thus the auto-oscillation amplitude continues to increase with increasing I_{dc} in the simulations, as shown in Fig. 5c. It has been demonstrated that nonlinear magnon scattering in S-SHOs increases with increasing ellipticity of the spin wave modes[25]. Given the nearly easy-xz-plane character of anisotropy in our SHO devices, one may expect low ellipticity of spin-wave modes and, thus, low nonlinear scattering rates in the standard mode of the SHO operation when the magnetic field is applied along the y-axis. However, the magnetic field in our experiment is applied at a significant angle with respect to the y-axis ($\phi_H = 68°$), and its magnitude is similar to the easy-xz-plane anisotropy field. This results in a significant ellipticity of spin-wave modes in the system and turns on the nonlinear scattering to thermal magnons. For this reason, the auto-oscillatory mode amplitude in the high-current regime decreases with increasing I_{dc} as seen in the experimental data in Fig. 3e.

Three major pathways to enhance the microwave power output of SOT oscillators are: (i) increase the amplitude of magnetization auto-oscillations, (ii) increase the conversion efficiency of magnetic oscillations into electric microwave signal and (iii) take advantage of phase locking in arrays of spin torque oscillators to harness phase coherence of their collective dynamics. While it is likely that the ultimate future high-power SOT oscillator devices will combine all three approaches, an important immediate task is to find optimal solutions to all three individual approaches prior to combining them into a device with the ultimate high-power performance. It is interesting to note that this problem has been largely solved for spin transfer torque oscillators where the large amplitude of magnetization oscillations is achieved in vortex-based oscillators[69], high conversion efficiency is achieved via tunneling magneto-resistance (TMR) in MTJs[70],

and phase locking of several of vortex oscillators has been demonstrated[71,72]. Achieving this degree of success is a grand challenge for SOT oscillators. If realized, this goal can lead to high-power SOT oscillator devices that are more energy-efficient than spin transfer torque oscillators and operate at higher microwave frequencies than vortex-based oscillators.

Our experimental demonstration of an EP-SHO solves the problem of achieving large-amplitude auto-oscillations in a single SOT oscillator. A common approach to increasing the amplitude of magnetic auto-oscillations in spin transfer torque devices is the excitation of auto-oscillations of a magnetic vortex[69]. However, vortex oscillators driven by spin Hall torque have not been realized due to the direction of the current polarization being in the FM|HM bilayer plane. The artificial EP approach shown to work in this paper presents a practical solution for large-amplitude SHO devices.

Recently, tunable PMA in an SHO based on a Pt|Co|Ni multilayer was used to decrease the detrimental nonlinear magnetic damping by minimizing the ellipticity of magnetization precession[25]. This SHO based on a 0.5 μm diameter disc was shown to operate with small nonlinear damping in the standard high-field SHO regime. However, the disc geometry does not support the artificial easy-xz-plane anisotropy demonstrated in this work.

The high conversion efficiency of magnetic auto-oscillations into electric microwave signals can be achieved in SHO devices with high magnetoresistance. To this end, the most promising approach is SHOs utilizing TMR, such as 3-terminal devices where a nanoscale MTJ is patterned on top of the HM material[7,73]. In such SHOs, the drive and the readout currents can be separately controlled, which allows for low power consumption combined with high output power. Another promising approach to boosting SHO output power while keeping Ohmic losses low utilizes current-in-plane giant magnetoresistance in a two-terminal device[50]. This approach takes advantage of the identical angular symmetries of spin Hall torque and giant magnetoresistance to simultaneously maximize the amplitude of resistance oscillations and spin Hall torque efficiency.

Finally, phase locking in one- and two-dimensional arrays of SHOs[14,74] has been experimentally demonstrated to significantly boost the SHO output power. Therefore, with the addition of the present work, all three individual components needed for making high-power SHO oscillator systems have been experimentally demonstrated. We thus expect that integrated SHO devices capable of generating the ultimate high microwave power are now within reach.

The artificial EP nanowire created by balancing the demagnetization energy with the PMA could serve as a convenient platform for hosting a spin texture referred to as a spin superfluid[75–77]. Such a texture can be created via injection of spin current polarized orthogonal to the EP of an FM, which leads to the generation and propagation of an exchange-mediated winding of the magnetic order parameter—the spin superfluid state. This winding is topologically robust and is predicted to carry long-range spin current[78,79]. The EP nanowire system presented here is potentially suitable for the excitation of spin superfluid by spin Hall torque applied to the active region and its propagation along the nanowire beyond the active region. However, our micromagnetic simulation show that spin superfluid is not excited due to spatial inhomogeneity of PMA induced by Ohmic heating of the active region. Further improvements of the device design via e. g. the use of magnetic materials with PMA that weakly depends on temperature may enable spin superfluid in this geometry.

In conclusion, our work provides the first experimental realization of an EP SHO. This oscillator can operate without a biased

magnetic field and generate high output microwave power due to the large amplitude of resistance auto-oscillations excited by spin Hall torque. The easy plane magnetic anisotropy perpendicular to the film plane is engineered by tuning the nanowire shape anisotropy and interfacial PMA. Our micromagnetic simulations of the oscillator performance are in good qualitative agreement with the measurements. Our results set the stage for the development of artificial spiking neurons driven by spin Hall torque[34] and for further enhancement of the oscillator output power via integration with a tunneling magnetoresistance readout[7,63].

Methods

Sample description. The multilayer films were deposited by dc magnetron sputtering on $Al_2O_3(0001)$ substrates in 2 mTorr of Ar process gas. A highly resistive, amorphous Ta seed layer was used to reduce film roughness and absorb spin Hall current from Pt propagating opposite to the Co|Ni superlattice. The highly resistive Ta cap was used to prevent oxidation of the Co|Ni. The multilayers were patterned into 50 nm wide, 40 μm long nanowires by means of electron-beam lithography using DOW-Corning HSQ negative resist and Ar ion mill etching. The electrical leads to the nanowire were patterned via electron-beam lithography using a methyl methacrylate/poly(methyl methacrylate) positive resist bilayer followed by the sputter deposition of Ta(5 nm)/Au(40 nm)/Ta(5 nm) and liftoff. The spacing between the leads defined an SHO active region ranging in length from 50 nm to 450 nm long in the central part of the nanowire.

Microwave emission measurements. The microwave power emitted from the SHO was detected using a standard circuit based on a microwave spectrum analyzer[56]. A direct current I_{dc} was applied to the sample through the low-frequency port of a bias tee. The signal from the SHO was amplified by a low-noise microwave amplifier with 45 dB gain, applied to the high-frequency port of the bias tee, and recorded by the microwave spectrum analyzer. For these measurements, the sample was placed in a He flow cryostat at a bath temperature of $T = 4.2$ K. The values of the microwave power reported here are those delivered to a 50 Ω load with the frequency-dependent circuit attenuation and amplification calibrated out. Resistance oscillations are calculated by treating the SHO as a mismatched microwave generator connected to a 50 Ω transmission line terminated with matched load (spectrum analyzer)[80].

Micromagnetic simulations. Micromagnetic simulations were made using the Mumax3 software. We simulate a 4 μm × 50 nm × 5.85 nm ferromagnetic nanowire composed of 2048 × 16 × 1 micromagnetic cells representing the length, width, and thickness, respectively. The simulations were made using the experimentally determined material parameters of the Co|Ni superlattice: saturation magnetization $M_s = 997$ emu cm^{-3} (997 kA m^{-1}), Gilbert damping $\alpha = 0.027$, and Landé g-factor $g = 2.18$. Exchange constant $A_{ex} = 1 \times 10^{-6}$ erg cm^{-1} (10 pJ m^{-1}) and spin Hall angle $\theta_{SH} = 0.07$ were used. Constant PMA of $H_{PMA} = 11.7$ kOe ($\mu_0 H_{PMA} = 1.17$ T) was used outside of the SHO active region. Current-dependent PMA was used in the SHO active region to capture the effects of Joule heating on anisotropy (see Supplementary Note 3 for details).

Data availability

All data generated or analyzed during this study are included in this published article and are available from the corresponding author upon reasonable request. Supplementary Movie 1, Supplementary Movie 2, and Supplementary Movie 3 are available for download.

References

1. Miron, I. M. et al. Perpendicular switching of a single ferromagnetic layer induced by in-plane current injection. *Nature* **476**, 189–193 (2011).
2. Liu, L. et al. Spin-torque switching with the giant spin Hall effect of tantalum. *Science* **336**, 555–558 (2012).
3. Baumgartner, M. et al. Spatially and time-resolved magnetization dynamics driven by spin–orbit torques. *Nat. Nanotechnol.* **12**, 980–986 (2017).
4. Sato, N., Xue, F., White, R. M., Bi, C. & Wang, S. X. Two-terminal spin–orbit torque magnetoresistive random access memory. *Nat. Electron.* **1**, 508–511 (2018).
5. Finocchio, G. et al. Spin–orbit torque based physical unclonable function. *J. Appl. Phys.* **128**, 033904 (2020).
6. Zheng, Z. et al. Field-free spin-orbit torque-induced switching of perpendicular magnetization in a ferrimagnetic layer with a vertical composition gradient. *Nat. Commun.* **12**, 4555 (2021).
7. Liu, L., Pai, C.-F., Ralph, D. C. & Buhrman, R. A. Magnetic oscillations driven by the spin Hall effect in 3-terminal magnetic tunnel junction devices. *Phys. Rev. Lett.* **109**, 186602 (2012).
8. Safranski, C., Montoya, E. A. & Krivorotov, I. N. Spin–orbit torque driven by a planar Hall current. *Nat. Nanotechnol.* **14**, 27–30 (2019).
9. Haidar, M. et al. A single layer spin-orbit torque nano-oscillator. *Nat. Commun.* **10**, 2362 (2019).
10. Sengupta, A., Azim, Z. A., Fong, X. & Roy, K. Spin-orbit torque induced spike-timing dependent plasticity. *Appl. Phys. Lett.* **106**, 093704 (2015).
11. Tsunegi, S. et al. Physical reservoir computing based on spin torque oscillator with forced synchronization. *Appl. Phys. Lett.* **114**, 164101 (2019).
12. Grollier, J. et al. Neuromorphic spintronics. *Nat. Electron.* **3**, 360–3701–11 (2020).
13. Hassan, O., Faria, R., Camsari, K. Y., Sun, J. Z. & Datta, S. Low-barrier magnet design for efficient hardware binary stochastic neurons. *IEEE Magn. Lett.* **10**, 1–5 (2019).
14. Zahedinejad, M. et al. Memristive control of mutual spin Hall nano-oscillator synchronization for neuromorphic computing. *Nat. Mater.* **21**, 81–87 (2022).
15. Demidov, V. E., Urazhdin, S., Anane, A., Cros, V. & Demokritov, S. O. Spin–orbit-torque magnonics. *J. Appl. Phys.* **127**, 170901 (2020).
16. Chumak, A. V. et al. Advances in magnetics roadmap on spin-wave computing. *IEEE Trans. Magn.* **58**, 1–72 (2022).
17. Barsukov, I. et al. Giant nonlinear damping in nanoscale ferromagnets. *Sci. Adv.* **5**, eaav6943 (2019).
18. Demidov, V. E. et al. Magnetic nano-oscillator driven by pure spin current. *Nat. Mater.* **11**, 1028–1031 (2012).
19. Duan, Z. et al. Nanowire spin torque oscillator driven by spin orbit torques. *Nat. Commun.* **5**, 5616 (2014).
20. Giordano, A. et al. Spin-Hall nano-oscillator: a micromagnetic study. *Appl. Phys. Lett.* **105**, 042412 (2014).
21. Smith, A. et al. Dimensional crossover in spin Hall oscillators. *Phys. Rev. B* **102**, 054422 (2020).
22. Zhang, H. et al. Spin-torque oscillation in a magnetic insulator probed by a single-spin sensor. *Phys. Rev. B* **102**, 024404 (2020).
23. Hache, T. et al. Bipolar spin Hall nano-oscillators. *Appl. Phys. Lett.* **116**, 192405 (2020).
24. Slavin, A. & Tiberkevich, V. Nonlinear auto-oscillator theory of microwave generation by spin-polarized current. *IEEE Trans. Magn.* **45**, 1875–1918 (2009).
25. Divinskiy, B., Urazhdin, S., Demokritov, S. O. & Demidov, V. E. Controlled nonlinear magnetic damping in spin-Hall nano-devices. *Nat. Commun.* **10**, 5211 (2019).
26. Lee, I., Zhang, C., Singh, S., McCullian, B. & Hammel, P. C. Origin of nonlinear damping due to mode coupling in auto-oscillatory modes strongly driven by spin-orbit torque. *Phys. Rev. Appl.* **17**, 064047 (2022).
27. Goto, M. et al. Uncooled sub-GHz spin bolometer driven by auto-oscillation. *Nat. Commun.* **12**, 536 (2021).
28. Kent, A. D., Özyilmaz, B. & del Barco, E. Spin-transfer-induced precessional magnetization reversal. *Appl. Phys. Lett.* **84**, 3897–3899 (2004).
29. Wang, X., Bauer, G. E. W. & Hoffmann, A. Dynamics of thin-film spin-flip transistors with perpendicular source-drain magnetizations. *Phys. Rev. B* **73**, 054436 (2006).
30. Rowlands, G. E. & Krivorotov, I. N. Magnetization dynamics in a dual free-layer spin-torque nano-oscillator. *Phys. Rev. B* **86**, 094425 (2012).
31. Firastrau, I. et al. Modeling of the perpendicular polarizer-planar free layer spin torque oscillator: micromagnetic simulations. *Phys. Rev. B* **78**, 024437 (2008).
32. Khymyn, R. et al. Ultra-fast artificial neuron: generation of picosecond-duration spikes in a current-driven antiferromagnetic auto-oscillator. *Sci. Rep.* **8**, 15727 (2018).
33. Matsumoto, R., Lequeux, S., Imamura, H. & Grollier, J. Chaos and relaxation oscillations in spin-torque windmill spiking oscillators. *Phys. Rev. Appl.* **11**, 044093 (2019).
34. Marković, D. et al. Easy-plane spin Hall nano-oscillators as spiking neurons for neuromorphic computing. *Phys. Rev. B* **105**, 014411 (2022).
35. Mangin, S. et al. Current-induced magnetization reversal in nanopillars with perpendicular anisotropy. *Nat. Mater.* **5**, 210–215 (2006).
36. Rippard, W. H. et al. Spin-transfer dynamics in spin valves with out-of-plane magnetized CoNi free layers. *Phys. Rev. B* **81**, 014426 (2010).
37. Mohseni, S. M. et al. High frequency operation of a spin-torque oscillator at low field. *Phys. Status Solidi RRL* **5**, 432–434 (2011).
38. Mohseni, S. M. et al. Spin torque–generated magnetic droplet solitons. *Science* **339**, 1295–1298 (2013).
39. Choi, J.-G. et al. Voltage-driven gigahertz frequency tuning of spin Hall nano-oscillators. *Nat. Commun.* **13**, 3783 (2022).
40. Macià, F., Backes, D. & Kent, A. D. Stable magnetic droplet solitons in spin-transfer nanocontacts. *Nat. Nanotechnol.* **9**, 992–996 (2014).

41. Lee, H. S. et al. Power-efficient spin-torque nano-oscillator-based wireless communication with CMOS high-gain low-noise transmitter and receiver. *IEEE Trans. Magn.* **55**, 1–10 (2019).

42. Torrejon, J. et al. Neuromorphic computing with nanoscale spintronic oscillators. *Nature* **547**, 428–431 (2017).

43. Flebus, B., Duine, R. A. & Hurst, H. M. Non-Hermitian topology of one-dimensional spin-torque oscillator arrays. *Phys. Rev. B* **102**, 180408 (2020).

44. Okamoto, S., Kikuchi, N., Furuta, M., Kitakami, O. & Shimatsu, T. Microwave assisted magnetic recording technologies and related physics. *J. Phys. D* **48**, 353001 (2015).

45. Sagasta, E. et al. Unveiling the mechanisms of the spin Hall effect in Ta. *Phys. Rev. B* **98**, 060410(R) (2018).

46. Berger, A. J. et al. Determination of the spin Hall effect and the spin diffusion length of Pt from self-consistent fitting of damping enhancement and inverse spin-orbit torque measurements. *Phys. Rev. B* **98**, 024402 (2018).

47. Arora, M., Hübner, R., Suess, D., Heinrich, B. & Girt, E. Origin of perpendicular magnetic anisotropy in Co/Ni multilayers. *Phys. Rev. B* **96**, 024401 (2017).

48. Montoya, E. et al. Spin transport in tantalum studied using magnetic single and double layers. *Phys. Rev. B* **94**, 054416 (2016).

49. Hoffmann, A. Spin Hall effects in metals. *IEEE Trans. Magn.* **49**, 5172–5193 (2013).

50. Chen, J.-R., Smith, A., Montoya, E. A., Lu, J. G. & Krivorotov, I. N. Spin–orbit torque nano-oscillator with giant magnetoresistance readout. *Commun. Phys.* **3**, 187 (2020).

51. Aharoni, A. Demagnetizing factors for rectangular ferromagnetic prisms. *J. Appl. Phys.* **83**, 3432–3434 (1998).

52. Montoya, E., McKinnon, T., Zamani, A., Girt, E. & Heinrich, B. Broadband ferromagnetic resonance system and methods for ultrathin magnetic films. *J. Magn. Magn. Mater.* **356**, 12–20 (2014).

53. Nakayama, H. et al. Spin Hall magnetoresistance induced by a nonequilibrium proximity effect. *Phys. Rev. Lett.* **110**, 206601 (2013).

54. Kim, J., Sheng, P., Takahashi, S., Mitani, S. & Hayashi, M. Spin Hall magnetoresistance in metallic bilayers. *Phys. Rev. Lett.* **116**, 097201 (2016).

55. Ando, K. et al. Electric manipulation of spin relaxation using the spin Hall effect. *Phys. Rev. Lett.* **101**, 036601 (2008).

56. Kiselev, S. I. et al. Microwave oscillations of a nanomagnet driven by a spin-polarized current. *Nature* **425**, 380–383 (2003).

57. Kiselev, S. I. et al. Current-induced nanomagnet dynamics for magnetic fields perpendicular to the sample plane. *Phys. Rev. Lett.* **93**, 036601 (2004).

58. Awad, A. A., Houshang, A., Zahedinejad, M., Khymyn, R. & Åkerman, J. Width dependent auto-oscillating properties of constriction based spin Hall nano-oscillators. *Appl. Phys. Lett.* **116**, 232401 (2020).

59. Vansteenkiste, A. et al. The design and verification of MuMax3. *AIP Adv.* **4**, 107133 (2014).

60. Krivorotov, I. N., Emley, N. C., Buhrman, R. A. & Ralph, D. C. Time-domain studies of very-large-angle magnetization dynamics excited by spin transfer torques. *Phys. Rev. B* **77**, 054440 (2008).

61. Devolder, T. et al. Chaos in magnetic nanocontact vortex oscillators. *Phys. Rev. Lett.* **123**, 147701 (2019).

62. Capriata, C. C. M., Jiang, S., Åkerman, J. & Malm, B. G. Impact of random grain structure on spin-Hall nano-oscillator modal stability. *IEEE Electron Device Lett.* **43**, 312–315 (2022).

63. Tarequzzaman, M. et al. Spin torque nano-oscillator driven by combined spin injection from tunneling and spin Hall current. *Commun. Phys.* **2**, 20 (2019).

64. McMichael, R. D. & Maranville, B. B. Edge saturation fields and dynamic edge modes in ideal and nonideal magnetic film edges. *Phys. Rev. B* **74**, 024424 (2006).

65. Cowburn, R. P., Koltsov, D. K., Adeyeye, A. O. & Welland, M. E. Lateral interface anisotropy in nanomagnets. *J. Appl. Phys.* **87**, 7067–7069 (2000).

66. Maranville, B. B., McMichael, R. D. & Abraham, D. W. Variation of thin film edge magnetic properties with patterning process conditions in Ni80Fe20 stripes. *Appl. Phys. Lett.* **90**, 232504 (2007).

67. Yang, L. et al. Parametric resonance of spin waves in ferromagnetic nanowires tuned by spin Hall torque. *Phys. Rev. B* **106**, 144410 (2022).

68. Demidov, V. E. et al. Control of magnetic fluctuations by spin current. *Phys. Rev. Lett.* **107**, 107204 (2011).

69. Pribiag, V. S. et al. Magnetic vortex oscillator driven by d.c. spin-polarized current. *Nat. Phys.* **3**, 498–503 (2007).

70. Tsunegi, S., Yakushiji, K., Fukushima, A., Yuasa, S. & Kubota, H. Microwave emission power exceeding 10 µW in spin torque vortex oscillator. *Appl. Phys. Lett.* **109**, 252402 (2016).

71. Ruotolo, A. et al. Phase-locking of magnetic vortices mediated by antivortices. *Nat. Nanotechnol.* **4**, 528–532 (2009).

72. Tsunegi, S. et al. Scaling up electrically synchronized spin torque oscillator networks. *Sci. Rep.* **8**, 13475 (2018).

73. Jué, E., Rippard, W. H. & Pufall, M. R. Comparison of the spin-transfer torque mechanisms in a three-terminal spin-torque oscillator. *J. Appl. Phys.* **124**, 043904 (2018).

74. Zahedinejad, M. et al. Two-dimensional mutually synchronized spin Hall nano-oscillator arrays for neuromorphic computing. *Nat. Nanotechnol.* **15**, 47–52 (2020).

75. Sonin, E. Spin currents and spin superfluidity. *Adv. Phys.* **59**, 181–255 (2010).

76. Yuan, W. et al. Experimental signatures of spin superfluid ground state in canted antiferromagnet Cr2O3 via nonlocal spin transport. *Sci. Adv.* **4**, eaat1098 (2018).

77. Stepanov, P. et al. Long-distance spin transport through a graphene quantum Hall antiferromagnet. *Nat. Phys.* **14**, 907–911 (2018).

78. Takei, S. & Tserkovnyak, Y. Superfluid spin transport through easy-plane ferromagnetic insulators. *Phys. Rev. Lett.* **112**, 227201 (2014).

79. Schneider, T. et al. Self-stabilizing exchange-mediated spin transport. *Phys. Rev. B* **103**, 144412 (2021).

80. Pozar, D. M. 2.6 Generator and Load Mismatches. in *Microwave Engineering*, 76–77 (Wiley, 2012), fourth edn.

Author contributions

E.A.M. developed and deposited the film structures, performed film-level measurements, and analyzed film-level data. E.A.M., C.S., and A.S. developed the nanofabrication process and made the nano-devices. C.S. and E.A.M. performed device-level measurements and analyzed device data. A.K. performed micromagnetic simulations. I.N.K. formulated and supervised the study. E.A.M., I.N.K., and A.K. wrote the paper. All authors discussed the results.

Competing interests

The authors declare no competing interests.

Additional information

Supplementary information The online version contains supplementary material available at https://doi.org/10.1038/s42005-023-01298-7.

Correspondence and requests for materials should be addressed to Eric Arturo Montoya or Ilya N. Krivorotov.

Peer review information *Communications Physics* thanks Roman Khymyn and the other anonymous reviewer(s) for their contribution to the peer review of this work. A peer review file is available.

Reprints and permission information is available at http://www.nature.com/reprints

Publisher's note Springer Nature remains neutral with regard to jurisdictional claims in published maps and institutional affiliations.